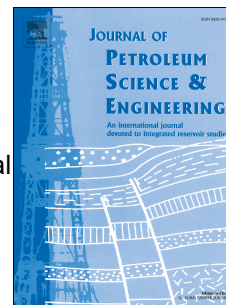# Accepted Manuscript

Multiphase flow in tight sandstone: An improved application for 3D intermingled fractal model

Caoxiong Li, Mian Lin, Lili Ji, Wenbin Jiang

Please cite this article as: Li, C., Lin, M., Ji, L., Jiang, W., Multiphase flow in tight sandstone: An improved application for 3D intermingled fractal model, *Journal of Petroleum Science and Engineering* (2019), doi: https://doi.org/10.1016/j.petrol.2019.02.030.

Multiphase flow in tight sandstone: an improved application for 3D intermingled fractal model

Caoxiong Li[a,b], Mian Lin[a,b]*,Lili Ji[a], Wenbin Jiang[a]

a. Institute of Mechanics, Chinese Academy of Sciences, Beijing 100190, China

b. School of Engineering Science, University of Chinese Academy of Sciences, Beijing 100049, China

*Corresponding author: linmian@imech.ac.cn

Abstract

Multiphase displacement in tight sandstone is fundamental and critical for tight oil production. Micropores dominate the pore space in tight sandstone. Microscopic mineral components in micropores substantially influence the multiphase displacement behavior. Pore size distribution exhibits a self-similar or fractal property, similar to inorganic mineral grains. Utilizing fractal theory eases the rebuilding of the flowing space and calculation of relative permeability. As an improvement of previous work, we successfully extended the 3D intermingled fractal model (3D IFM). The extended 3D IFM can evaluate multiphase flow behavior in tight sandstone, considering fractal characteristics of pore size distribution and mineral grain distribution. The fractal information of pores and mineral properties are obtained by scalable scanning electron microscopy (SEM) and energy dispersive spectroscopy（EDS） images, respectively. This method is useful and reliable for calculating relative permeability and residual saturation. The method is also successfully used to evaluate the influence of oil-water viscosity ratio, mineral components and formation depth on multiphase displacement behavior, proving its convenience and potential in rapidly evaluating multiphase displacement behavior in tight sandstone.

Keywords

Tight sandstone; Fractal; Mineral component; Multiphase displacement

1 Introduction

Most tight oils are contained in petroleum-bearing formations with tight matrix and low permeability. Tight matrices often contain an assemblage of rocks, reservoirs, and caprocks. Tight sandstone is a commonly discovered tight matrix. During economic production from tight sandstone formation, hydraulic fracturing is commonly used to enhance recovery. In hydraulic fracturing and flowback, multiphase displacement behavior between oil and fracturing liquid will considerably influence the

production. Tight sandstone features relatively low permeability and porosity compared with conventional sandstone; it commonly presents a gas permeability of less than 0.1 mD [1-2] and pore throat sizes ranging from approximately 0.03 μm to 2 μm[3]. Tight sandstones exhibit a complex and unique multiphase displacement mechanism. Non-Darcy effect, that is, the deviation form linear relation between flow velocity and pressure gradient, becomes notable as pore throat diameter decreases from the macro to micro scale. Wetting behavior, caused by the component and distribution of a variety of mineral grains, will also remarkably influence oil–water displacement behavior in micropores. The influence becomes perceptible in tight sandstone owing to the high capillary force in the matrix. Given the complex flow mechanism in tight sandstone, the multiphase displacement mechanism and rapid evaluation of relative permeability should be investigated for the analysis of oil production, hydraulic fracturing, and production forecasting, and may helpful for drilling and carbonate

Multiphase displacement, especially oil–water displacement, is a fundamental problem for tight sandstone reservoir development. Evaluating oil–water relative permeability curve is a key problem that requires research attention. However, the network of pore space should first be rebuilt precisely and effectively. The pore space of tight sandstone differs from that of conventional sandstone. Tight sandstone is relatively heterogeneous and features relatively low connectivity and complicated pore structure[4]. The characteristics of pore structure and pressure condition has significant influence on multi-phase displacement behavior, which has been studied for several years [5-10]. On the basis of effective pore network model, multiphase displacement behavior is calculated by introducing the capillary force, non-Darcy effect, and wettability behavior. Since Fatt[11] first combined the parallel tube bundle based on actual pore size distribution with the network model, various models have been developed over the years. Bryant et al. [12-13] presented a predictive calculation of two-phase relative permeability in equivalent network for granular porous media by considering stress deformation. Blunt [14] built a 3D equilibrium-based pore level network model to compute relative permeability and capillary pressure for drainage and imbition cycles. Mani and Mohanty[15] extended the model into three-phase displacement. Dixit et al.[16] studied hysteresis phenomena and relative permeability curve by using a modified 3D rectangular network model. Related similar models are developed by Fishcher and Celia[17], Valvatne and Blunt[18], Yuan[19] and Lu et al[20]. Bakke and Øren[21] developed a 3D random network that is more realistic than a regular network. Nguyen et al.[22] developed a dynamic network model that combines the complex interaction among displacement rate,

contact angle, aspect ratio, and pore and throat shapes on relative permeability. Recently, Ren et al.[23] developed an improved

analytical oil–water displacement model to analyze nonlinear seepage characteristics in tight sandstone and verified the model

with experiments.

Deterministic fractal is a geometric figure whose each and every part is similar to the whole, and that is repeated on different

scales. Pores in tight sandstone possess fractal properties at a certain scale [24], similar to mineral grains[25]. The fractal theory

conveniently represents complicated pore space and mineral grains by using self-similar properties[26-27]. Toledo et al [28]

investigated the scaling laws between fractal dimension and capillary pressure and between fractal dimension and relative

permeability of the wetting phase in sandstones. Cai et al. [29-31] used the fractal theory to calculate multiphase flowing behavior

and applied the model in several applications. Xiao et al [32] and Xu et al[33] combined fractal and Monte Carlo method to

predict the relative permeability of unsaturated porous media. Lei et al. [34] introduced fractal tortuosity into a tube bundle model

to investigate stress-dependent relative permeability in sandstone. Balankin et al.[35-36] developed a fractal continuum model to

calculate the flow process in random fractal porous media. Pia and Sanna[37] were the first to build an intermingled fractal unit

(IFU) method for representing multi-fractal behavior of pore structure; the author also developed various applications in

multiphase displacement process[38-40]. Cihan et al.[41-42] developed a new method, called the probabilistic capillary

connectivity (PCC) method, to calculate permeability and relative permeability in 3D random fractal media. This method

creatively represents the pore connectivity with connective probability. Recently, Li et al.[43] successfully combined the IFU

model and PCC method to calculate shale permeability.

2 Basic theory of the fractal model and relative permeability calculation

2.1 Introduction of 3D IFU

First developed by Pia and Sanna[37], the IFU model represents random pores in porous media. The model is a combination

of several randomized multi-fractal sub-units. These sub-units are revised from the basic Sierpinski carpet model. Pia and

Sanna[37] have defined and explained in detail the IFU model in their work. Additionally, the PCC method, developed by Cihan

et al.[41-42, 44], calculates the permeability of randomized Menger sponge. Previously, we have successfully developed a 3D

intermingled fractal model (3D IFM) by combining revised IFU and PCC method and calculated the apparent permeability for

shale[43]. In the present work, we expand the previous model into multiphase calculation and introduce mineral components to calculate the displacement process in tight sandstone. Background information about model suggestions and basic parameter definitions can be found in the related references above. This information clarifies the 3D IFU model for comprehensibility. The general governing equation for unsteady state flow can be expressed as:

$$\begin{cases} div\left(\dfrac{K_{nw}}{\mu_{nw}}\, gradP_{nwr}\right) = \phi\dfrac{\partial S_{nw}}{\partial t} \\ div\left(\dfrac{K_w}{\mu_w}\, gradP_{wr}\right) = \phi\dfrac{\partial S_w}{\partial t} \end{cases} \qquad\qquad (1)$$

The general governing equation for steady state flow can be expressed as:

$$\begin{cases} \dfrac{K_{nw}}{\mu_{nw}}\, gradP_{nwr} = \phi S_{nw}\bar{v}_{nw} \\ \dfrac{K_w}{\mu_w}\, gradP_{wr} = \phi S_w\bar{v}_w \end{cases} \qquad\qquad (2)$$

where 'nw' and 'w' means non-wetting phase and wetting phase; K_{nw} and K_w are permeability of non-wetting phase and wetting phase; μ_{nw} and μ_w are viscosity; P_{nwr} and P_{wr} are pressure difference; S_{nw} and S_w are saturation; $\bar{v}_{nw}$ and $\bar{v}_w$ are average velocity, controlled by Poiseuille equation; ϕ is porosity and t is time.

2.2 Multiphase probabilistic capillary connectivity (PCC) method

In this section, we extend the basic PCC method into relative permeability calculation in 3D IFU. The basic theory about PCC method is provided by Marshall et al.[45] and Cihan et al.[41]. In PCC method, connecting probabilities for pores in any cross section of sponge are assumed equal, that is, large pores will gain high connecting probability, thereby indicating high permeability.

In this work, our primary concern is to link PCC with relative permeability calculation and consider several mineral ingredients with different wetting behavior. To simplify the problem, we assume the following simplifications. a) Pores and bulks are squares/necks corrected with shape factors on cross section. b) Permeability is related to connecting probability in fractal porous media. c) Pores and bulks in 3D space feature random distributions. d) The number of pores is sufficient; thus, cross sections share the same fractal dimension and pore size distribution. e) Each mineral possesses its own wettability behavior, and mixed wetting is neglected. Fig.1 shows the schematic diagram for this displacement process.

Multiphase flow is more complicated than the single-phase one. As a result, multiphase introduces new problems, such as Jamin effect, dynamic meniscus behavior, and non-Darcy flow. To calculate the relative permeability of 3D IFU, we introduce two parameters: connected fraction P_1 and traverse probability P_2.

The connected fraction $P_{1,i}$ is the fraction of connecting pores (except dead ends) existing at i th iteration level and is a decimal between 0 and 1. For example, given N_i pores at i th iteration level during the iterating process, $< N_i(1-P_{1,i}) >$ pores are dead ends; only $< N_i P_{1,i} >$ pores will participate in the multiphase displacement process. The angle brackets '$< >$' are a symbol of nearest integer function, and they are used to keep the number of pores as integer. For real sandstone, P_1 at each iteration level can be easily derived from the capillary pressure–saturation (Pc–Sw) curve comparison between mercury injection experiment and CT or SEM data. The Pc–Sw curve derived from mercury injection denotes the connected pores, whereas that observed and simulated from CT or SEM data comprises all pores. Specifically, we first obtain the observed pore size distribution information from CT or SEM data. Then, we use the IFU model to match the real size distribution and obtain simulated fractal distribution. Finally, we utilize simulated fractal pore size distribution to calculate the simulated Pc–Sw curve. With the existence of dead ends, this Pc–Sw curve will usually show no matching the mercury injection Pc–Sw curve. Therefore, in each iteration level, we introduce and adjust the connected fraction P_1 to narrow down the differences in fractal and mercury Pc–Sw curves. Finally, the introduced P_1 corrects the influence of dead ends in porous media.

The traverse probability P_2 is the probability of meniscus travel over the pore neck. P_2 is influenced by several forces, such as driving force, capillary force, and friction from walls. We set $P_{2,i \to j}$ as the traverse probability from pore neck at iteration level i to iteration level j. If the driving force is larger than the resistance, then the meniscus can travel over the pore neck. Thus, $P_{2,i \to j} = 1$; otherwise, $P_{2,i \to j} = 0$. To successfully complete a multiphase displacement at pore neck, two conditions must be met. First, the pores should be connected at pore neck (controlled by PCC). Second, the injected liquid should gain enough energy (driving force larger than resistance) to overcome resistance at pore neck.

We conduct three steps to calculate relative permeability on the basis PCC method, shown in Fig.2. First, we calculate the pore connective probability, followed by traverse probability and relative permeability. To calculate the pore connective probability, we build the probability calculation table according to Table 1. The table is rearranged in accordance with the

descending order of pore diameters. The largest pore is λ_1, where the number of pores is N_1. Only $< N_1 P_{1,1} >$ pores participate

in the displacement process. Hence, the probability of λ_1 pores in one surface (face A) connecting to other λ_1 pores in other

surfaces (face B) is $(\lambda_1^2 < N_1 P_{1,1} > / A)^2$, which is called connecting probability. A refers to the cross-sectional area of

porous media. To calculate traverse probability, driving forces and resistance are compared. If the driving force is large, then

meniscus can travel over the pore neck. Therefore, $P_{2,i\to j} = 1$. Otherwise, meniscus will be arrested at pore neck, that is,

$P_{2,i\to j} = 0$. Thus, the general connecting and successful displacement probability P_{CSDP} for iteration level 1 is as follows:

$$P_{CSDP,1} = (\lambda_1^2 < N_1 P_{1,1} > / A)^2 \times P_{2,1\to1}, \dots\dots\dots\dots\dots\dots\dots\dots\dots\dots\dots\dots\dots\dots\dots\dots (3)$$

shown in Table 1. Similarly, at the second iteration level, the number of effective pores at level 2 is $< N_2 P_{1,2} >$, and number of

dead ends is $< N_2 (1 - P_{1,2}) >$. At this level, according to PCC theory[41], the general probability is combined by the following

three parts. First, the probability of λ_2 pores in face A connecting to λ_2 pores in face B is $(\lambda_2^2 < N_2 P_{1,2} > / A)^2 \times P_{2,2\to2}$.

Second, the probability of λ_1 pores in face A connecting to λ_2 pores in face B is

$(\lambda_1^2 < N_1 P_{1,1} > / A) \times (\lambda_2^2 < N_2 P_{1,2} > / A) \times P_{2,1\to2}$. Third, the probability of λ_2 pores in face A connecting to λ_1 pores in

face B is $(\lambda_2^2 < N_2 P_{1,2} > / A) \times (\lambda_1^2 < N_1 P_{1,1} > / A) \times P_{2,2\to1}$. In summary, the general connecting and successful

displacement probability P_{CSDP} for iteration level 2 is computed by the following:

$$P_{CSDP,2} = \frac{\lambda_2^2 < N_2 P_{1,2} >}{A} \frac{\lambda_2^2 < N_2 P_{1,2} >}{A} P_{2,2\to2} + \frac{\lambda_1^2 < N_1 P_{1,1} >}{A} \frac{\lambda_2^2 < N_2 P_{1,2} >}{A} P_{2,1\to2} + \frac{\lambda_1^2 < N_1 P_{1,1} >}{A} \frac{\lambda_2^2 < N_2 P_{1,2} >}{A} P_{2,2\to1}, \dots (4)$$

shown in Table 1. Similarly, we can obtain P_{CSDP} in the following iteration levels.

In accordance with the definition of $P_{2,i\to j}$, we can give the detailed equation for $P_{2,i\to j}$. By considering force

displacement (non-wetting phase driving wetting phase) as an example, capillary force acts as a resistance. Hence, $P_{2,i\to j}$ is

calculated as follows:

$$P_{2,i\to j} = \begin{cases} 1 & (\Delta P - P_c - (32\mu_{nw}L_p / \lambda_i^2 + P_{initial}) - 32\mu_w(L - L_p)/\lambda_j^2 - P_G > 0) \\ 0 & (\Delta P - P_c - (32\mu_{nw}L_p / \lambda_i^2 + P_{initial}) - 32\mu_w(L - L_p)/\lambda_j^2 - P_G < 0) \end{cases}, \dots\dots\dots\dots\dots (5)$$

In imbibition, capillary force acts as a driving force. Therefore, $P_{2,i\to j}$ is represented by the following:

$$P_{2,i\to j} = \begin{cases} 1 & (\Delta P + P_c - (32\mu_{nw}L_p / \lambda_i^2 + P_{initial}) - 32\mu_w(L - L_p)/\lambda_j^2 - P_G > 0) \\ 0 & (\Delta P + P_c - (32\mu_{nw}L_p / \lambda_i^2 + P_{initial}) - 32\mu_w(L - L_p)/\lambda_j^2 - P_G < 0) \end{cases}. \dots\dots\dots\dots\dots (6)$$

where ΔP denotes the pressure difference between inlet and outlet of model; μ_{nw} and μ_w refer to the viscosity of non-wetting

and wetting phases, respectively; $P_{initial}$ corresponds to the threshold pressure gradient, whose useful expression is provided by

Tian et al[46]; L identifies the edge length of model; setting cross section is perpendicular to injection direction; L_p specifies the

distance from cross section to pressure inlet and regarded as the average length of each iteration level in the invasion part; P_G

represents a projection of gravity on flow direction (when gravity is perpendicular to flow direction, gravity is neglected), and it

can normally be neglected in tight porous media; P_c is the capillary pressure, $P_c = \sigma \tilde{C}_n / (\lambda_i / 2)$; σ is the interfacial tension

between two fluid phases; According to Ma et al.[47], $\tilde{C}_n$ is the curvature of a meniscus:

$$\tilde{C}_n = \begin{cases} 2\cos\theta_R & (90° - \alpha < \theta_R < 90°) \\ \cos\theta_R + \sqrt{\dfrac{\tan\alpha}{2}\left[\sin 2\theta_R + \pi(1 - \dfrac{\alpha + \theta_R}{90})\right]} & (\theta_R < 90° - \alpha) \end{cases} \quad \dots\dots\dots\dots(7)$$

where α is the half angle of the corner, that is, $\alpha = 45°$ for a square cross section; θ_R denotes the dynamic contact angle, such

as advancing and receding angle. The advancing and receding angle is controlled by capillary number, C_a.

$$C_a = \mu v / \sigma, \dots\dots\dots\dots\dots\dots\dots\dots\dots\dots\dots\dots\dots\dots\dots\dots(8)$$

C_a controlled by viscosity μ, interfacial tension σ and velocity. Technically, the dynamic contact angle shows a slight

difference with the static contact angle. Hilpert [48-52] gives an expression about dynamic contact angle as:

$$\cos\theta_R - \cos\theta_{eq} = \tilde{\alpha} C_a^{\tilde{\beta}}, \dots\dots\dots\dots\dots\dots\dots\dots\dots\dots\dots\dots\dots\dots(9)$$

where θ_{eq} is static contact angle. $\tilde{\alpha}, \tilde{\beta}$ are dimensionless parameters. Hilpert introduced the definition and common value of

$\tilde{\alpha}, \tilde{\beta}$ in detail. On the basis of published experimental data and related conclusions [53-55], when capillary number $C_a > 10^{-5}$,

the dynamic contact angle varies with velocity, and when $C_a < 10^{-5}$, $\tilde{\beta}$ approaches to 0, contact angle becomes a velocity-

independent parameter. Given the relative slow displacement in tight media, we set dynamic contact angle as a velocity-

independent parameter in this work.

Displacement efficiency is remarkably influenced by residual oil saturation. During and after the displacement process,

certain residual phases will remain in corners. Several studies have provided residual saturation models[56]. We select the Ma's

residual saturation model[47], which provides the relationship between residual wetting phase $S_{wres}(\alpha, \theta_R)$ and shape of cross

section:

$$S_{wres}(\alpha, \theta_R, i) = \frac{\tan\alpha}{C_n^2}\left[\frac{\cos\theta_R}{\sin\alpha}\cos(\alpha + \theta_R) - \frac{\pi}{2}(1 - \frac{\alpha + \theta_R}{90})\right] \dots\dots\dots\dots\dots\dots(10)$$

In summary, by considering the force injection process (non-wetting phase driving wetting phase in wetting-phase-saturated matrix, or primary drainage) as an example, we derive relative permeability in 3D IFU model as follows:

For iteration level i=1, the following are utilized:

$$k_{nw\_sub}(1) = C_1 \frac{\lambda_1^2 < N_1 P_{1,1} >}{A} \frac{\lambda_1^2 < N_1 P_{1,1} >}{A} \lambda_1^2 P_{2,1\to1}, \dots \dots \dots \dots \dots \dots \dots (11)$$

$$k_{w\_sub}(1) = C_1 \frac{\lambda_1^2 < N_1 P_{1,1} >}{A} \frac{\lambda_1^2 < N_1 P_{1,1} >}{A} \lambda_1^2 (1 - P_{2,1\to1}), \dots \dots \dots \dots \dots \dots \dots (12)$$

where C_1 refers to the shape factor[29,56]; $k_{nw\_sub}(1)$ represents the non-wetting phase permeability at iteration level i=1; $k_{w\_sub}(1)$ corresponds to the wetting phase permeability at iteration level i=1. Non-wetting phase residual saturation left in the first level pores is computed as follows:

$$S_{nw\_sub}(1) = \frac{\lambda_1^2 < N_1 P_{1,1} > P_{2,1\to1}[1 - S_{wres}(\alpha,\theta,1)]}{\sum_{i=1}^n \lambda_i^2 P_{1,i}} \dots \dots \dots \dots \dots \dots \dots (13)$$

For iteration level i=2, the following are employed:

$$k_{nw\_sub}(2) = C_2 \lambda_2^2 \left[\begin{array}{l} \frac{\lambda_2^2 < N_2 P_{1,2} >}{A} \frac{\lambda_2^2 < N_2 P_{1,2} >}{A} P_{2,2\to2} + \frac{\lambda_1^2 < N_1 P_{1,1} >}{A} \frac{\lambda_2^2 < N_2 P_{1,2} >}{A} P_{2,1\to2} \\ + \frac{\lambda_1^2 < N_1 P_{1,1} >}{A} \frac{\lambda_2^2 < N_2 P_{1,2} >}{A} P_{2,2\to1} \end{array} \right], \dots (14)$$

$$k_{w\_sub}(2) = C_2 \lambda_2^2 \left[\begin{array}{l} \frac{\lambda_2^2 < N_2 P_{1,2} >}{A} \frac{\lambda_2^2 < N_2 P_{1,2} >}{A} (1 - P_{2,2\to2}) + \frac{\lambda_1^2 < N_1 P_{1,1} >}{A} \frac{\lambda_2^2 < N_2 P_{1,2} >}{A} (1 - P_{2,1\to2}) \\ + \frac{\lambda_1^2 < N_1 P_{1,1} >}{A} \frac{\lambda_2^2 < N_2 P_{1,2} >}{A} (1 - P_{2,2\to1}) \end{array} \right], \quad (15)$$

$$S_{nw\_sub}(2) = \frac{\lambda_2^2 < N_2 P_{1,2} > (P_{2,1\to2} + P_{2,2\to1} + 2P_{2,2\to2})/4 \times [1 - S_{wres}(\alpha,\theta,2)]}{\sum_{i=1}^n \lambda_i^2 P_{1,i}} \quad (16)$$

For iteration level i=3, the following equations are used:

$$k_{nw\_sub}(3) = C_3 \lambda_3^2 \left[\begin{array}{l} \frac{\lambda_3^2 < N_3 P_{1,3} >}{A} \frac{\lambda_3^2 < N_3 P_{1,3} >}{A} P_{2,3\to3} + \frac{\lambda_1^2 < N_1 P_{1,1} >}{A} \frac{\lambda_3^2 < N_3 P_{1,3} >}{A} (P_{2,1\to3} + P_{2,3\to1}) \\ + \frac{\lambda_2^2 < N_2 P_{1,2} >}{A} \frac{\lambda_3^2 < N_3 P_{1,3} >}{A} (P_{2,2\to3} + P_{2,3\to2}) \end{array} \right], \quad (17)$$

$$k_{w\_sub}(3) = C_3 \lambda_3^2 \left[\begin{array}{l} \dfrac{\lambda_3^2 < N_3 P_{1,3} >}{A} \dfrac{\lambda_3^2 < N_3 P_{1,3} >}{A}(1 - P_{2,3\to3}) + \dfrac{\lambda_1^2 < N_1 P_{1,1} >}{A} \dfrac{\lambda_3^2 < N_3 P_{1,3} >}{A}(2 - P_{2,1\to3} - P_{2,3\to1}) \\ + \dfrac{\lambda_2^2 < N_2 P_{1,2} >}{A} \dfrac{\lambda_3^2 < N_3 P_{1,3} >}{A}(2 - P_{2,2\to3} - P_{2,3\to2}) \end{array} \right] \quad (18)$$

$$S_{nw\_sub}(3) = \frac{\lambda_3^2 < N_3 P_{1,3} > (P_{2,1\to3} + P_{2,3\to1} + P_{2,2\to3} + P_{2,3\to2} + 2P_{2,3\to3})/6 \times (1 - S_{wres}(\alpha,\theta,3))}{\sum\limits_{i=1}^{n} \lambda_i^2 P_{1,i}} . \quad (19)$$

Similarly, for iteration level i=n, the following are utilized:

$$k_{nw\_sub}(n) = \left[\begin{array}{l} \dfrac{\lambda_n^2 < N_n P_{1,n} >}{A} \dfrac{\lambda_n^2 < N_n P_{1,n} >}{A} P_{2,n\to n} + \dfrac{\lambda_1^2 < N_1 P_{1,1} >}{A} \dfrac{\lambda_n^2 < N_n P_{1,n} >}{A}\left(P_{2,1\to n} + P_{2,n\to1}\right) \\ + \dfrac{\lambda_2^2 < N_2 P_{1,2} >}{A} \dfrac{\lambda_n^2 < N_n P_{1,n} >}{A}\left(P_{2,2\to n} + P_{2,n\to2}\right) + \ldots \\ + \dfrac{\lambda_{n-1}^2 < N_{n-1} P_{1,n-1} >}{A} \dfrac{\lambda_n^2 < N_n P_{1,n} >}{A}\left(P_{2,n-1\to n} + P_{2,n\to n-1}\right) \end{array} \right] C_n \lambda_n^2, \quad (20)$$

$$k_{w\_sub}(n) = \left[\begin{array}{l} \dfrac{\lambda_n^2 < N_n P_{1,n} >}{A} \dfrac{\lambda_n^2 < N_n P_{1,n} >}{A}\left(1 - P_{2,n\to n}\right) + \dfrac{\lambda_1^2 < N_1 P_{1,1} >}{A} \dfrac{\lambda_n^2 < N_n P_{1,n} >}{A}\left(2 - P_{2,1\to n} - P_{2,n\to1}\right) \\ + \dfrac{\lambda_2^2 < N_2 P_{1,2} >}{A} \dfrac{\lambda_n^2 < N_n P_{1,n} >}{A}\left(2 - P_{2,2\to n} - P_{2,n\to2}\right) + \ldots \\ + \dfrac{\lambda_{n-1}^2 < N_{n-1} P_{1,n-1} >}{A} \dfrac{\lambda_n^2 < N_n P_{1,n} >}{A}\left(2 - P_{2,n-1\to n} - P_{2,n\to n-1}\right) \end{array} \right] C_n \lambda_n^2, \quad (21)$$

$$S_{nw\_sub}(n) = \frac{\lambda_n^2 < N_n P_{1,n} > \sum\limits_{i=1}^{n} \dfrac{(P_{2,i\to n} + P_{2,n\to i})}{2n} \times [1 - S_{wres}(\alpha,\theta,n)]}{\sum\limits_{i=1}^{n} \lambda_i^2 P_{1,i}} . \quad (22)$$

To sum up, the permeabilities for non-wetting and wetting phases in 3D IFU are respectively calculated as follows:

$$k_{nw}(n) = \sum_{i=1}^{n} k_{nw\_sub}(i) , \quad (23)$$

$$k_{w}(n) = \sum_{i=1}^{n} k_{w\_sub}(i) . \quad (24)$$

Relative permeability denotes the ratio of apparent permeability to instinct permeability. The instinct permeability of 3D IFM is the case when all pores are filled with a single phase with normal Darcy flow. Based on Cihan et al.[41] and Li et al.[43], instinct Darcy permeability for 3D IFM is calculated as follows:

$$k_{ins}(n) = \frac{\lambda_1^2 N_1}{A} \frac{\lambda_1^2 N_1}{A} C_1 \lambda_1^2 + \left(\frac{\lambda_2^2 N_2}{A} \frac{\lambda_2^2 N_2}{A} + 2 \times \frac{\lambda_1^2 N_1}{A} \frac{\lambda_2^2 N_2}{A} \right) C_2 \lambda_2^2$$

$$+ \left(\frac{\lambda_3^2 N_3}{A} \frac{\lambda_3^2 N_3}{A} + 2 \times \frac{\lambda_1^2 N_1}{A} \frac{\lambda_3^2 N_3}{A} + 2 \times \frac{\lambda_2^2 N_2}{A} \frac{\lambda_3^2 N_3}{A} \right) C_3 \lambda_3^2 + \dots \qquad (25)$$

$$+ \left(\frac{\lambda_n^2 N_n}{A} \frac{\lambda_n^2 N_n}{A} + 2 \times \sum_{i=1}^{n-1} \frac{\lambda_i^2 N_i}{A} \frac{\lambda_n^2 N_n}{A} \right) C_n \lambda_n^2$$

The relative permeability for non-wetting and wetting phases in 3D IFU model are respectively computed as follows:

$$k_{r\_nw}(n) = \frac{k_{nw}(n)}{k_{ins}(n)}, \qquad (26)$$

$$k_{r\_w}(n) = \frac{k_w(n)}{k_{ins}(n)}. \qquad (27)$$

The saturation for non-wetting and wetting phases in 3D IFU model are respectively given by the following:

$$S_{nw}(n) = \sum_{i=1}^{n} S_{nw\_sub}(i), \qquad (28)$$

$$S_w(n) = 1 - S_{nw}(n). \qquad (29)$$

In general, the formula to describe multiphase displacement process under IFM method can be expressed as:

$$k_{nw}(n) = \frac{\sum_{j=1}^{n} \left\{ \left[\sum_{i=1}^{j} \frac{\lambda_i^2 <N_i P_{1,i}>}{A} \frac{\lambda_j^2 <N_j P_{1,j}>}{A} C_i \left(2 - P_{2,i \to j} + P_{2,j \to i} \right) - \left(\frac{\lambda_j^2 <N_j P_{1,j}>}{A} \right)^2 C_i (1 - P_{2,j \to j}) \right] \lambda_j^2 \right\}}{\sum_{j=1}^{n} \left[\left(2 \sum_{i=1}^{j} \left(\frac{\lambda_i^2 N_i}{A} \frac{\lambda_j^2 N_j}{A} \right) - \frac{\lambda_j^2 N_j}{A} \frac{\lambda_j^2 N_j}{A} \right) C_j \lambda_j^2 \right]} \qquad (30)$$

$$k_w(n) = \frac{\sum_{j=1}^{n} \left\{ \left[\sum_{i=1}^{j} \frac{\lambda_i^2 <N_i P_{1,i}>}{A} \frac{\lambda_j^2 <N_j P_{1,j}>}{A} C_i \left(P_{2,i \to j} + P_{2,j \to i} \right) - \left(\frac{\lambda_j^2 <N_j P_{1,j}>}{A} \right)^2 C_i P_{2,j \to j} \right] \lambda_j^2 \right\}}{\sum_{j=1}^{n} \left[\left(2 \sum_{i=1}^{j} \left(\frac{\lambda_i^2 N_i}{A} \frac{\lambda_j^2 N_j}{A} \right) - \frac{\lambda_j^2 N_j}{A} \frac{\lambda_j^2 N_j}{A} \right) C_j \lambda_j^2 \right]} \qquad (31)$$

3 Building the intermingled fractal model (IFM) for tight sandstone

3.1 Basic information

In this section, we discuss how to build the 3D IFM for real sandstone sample and the IFM for real samples on the basis of experimental data. Tight sandstone exhibits a relatively complicated pore space. Various factors, such as pore structure, mineral component, wettability behavior, and non-Darcy effect, influence multiphase displacement behavior. In this study, we use a real tight sandstone sample to build a 3D IFM and calculate the relative permeability. Pore size distribution information is obtained by

scalable scanning electron microscopy (SEM) images. Mineral components are determined by conducting energy dispersive

spectroscopy (EDS) test. The information on connected pores and dead ends are obtained via mercury intrusion method.

Combining all information together, we can establish the 3D IFM and calculate the relative permeability finally.

The sample is a fresh core sample from a tight-oil well in tight sandstone formation from Xinjiang. To obtain the pore

distribution, we polish the sample using argon ion. Then, we subject the sample to scalable SEM test. Rock mineralogy of samples

is analyzed in an area of 400 µm x 400 µm by using a Zeiss–Merlin rock mineralogy analysis machine with a maximal resolution

of 4 nm. The results are shown in Fig.3. As observed through the SEM images, micropores are dominant in tight sandstone,

featuring several pore types, such as interparticle pores, quartz dissolution pores and clay mineral-dominated pores. Fractal

properties of these inorganic pores can be derived from image analysis and statistics. In addition, within the same analysis area of

the sample, we conduct EDS test to derive the mineral component information. The analysis area of EDS is 400 µm x 400 µm

with a resolution of approximately 1 µm.

3.2 Fractal representation for micropores.

Tight sandstone contains abundant interparticle and intraparticle pores. Fig.4. shows the detailed IFU modeling process. The

building process is similar with IFU foundation processes in previous works ([40,43,58]). We list the steps briefly as follows:

In scalable SEM images, the first step is to calculate the representative elementary surface (RES) for pores by extending the

method, as commonly observed in previous works. As the target subarea extends, the average grayscale in subarea is calculated

simultaneously. When the average grayscale stabilizes, the subarea is regarded as RES. In this sandstone sample, the area of 400

µm × 400 µm reaches the RES. The next step is to adjust the pores from SEM images in scalable SEM images. After

segmentation, the grayscale image becomes binarized. The pore cumulative distribution curve of the samples is then derived.

Finally, within the binarized image, we adjust the fractal parameters to narrow the differences in cumulative curves between the

basic IFU model and image calculation. Finally, certain parameters of the 3D IFU model are determined. The parameters are

shown in Table 2. Also, CT images is an alternate fractal information source. The following building steps are similar with SEM

images.

Tight sandstone consists of several mineral grains, such as quartz, albite, dolomite, orthoclase, and illite. During displacement, the wettability of these grains substantially influences the relative permeability and residual distribution. Each mineral features its own wettability property. Displacement behavior is notably influenced by wettability. Therefore, rebuilding multi-fractal pores with unique contact angle is insufficient. Mineral wettability should be attached on the surface of 3D IFM. We use the EDS to gain mineral component information for tight sandstone. The EDS image shares the same target area with the SEM image. The resolution is 200 nm. The EDS results are shown in Fig.5.

In the EDS image, the distribution of mineral grains shows a self-similar or fractal property. The IFU model represents mineral grains well. Fig.6 shows the majority of minerals in this tight sandstone sample. The dominant minerals include quartz, albite, dolomite, orthoclase and illite, accounting for 92.36% of total mineral component. We select the top four minerals to rebuild the mineral space in this study. Similar with previous work, quartz is a base mineral that gains fractal parameters for other minerals separately. Then, we build a base mineral cube (quartz for this sample) and randomly scatter IFUs for albite, dolomite and orthoclase into the base cube. In this manner, IFU blocks will replace the original base mineral, and no overlapping will be observed with the scattered mineral blocks. Finally, we derive the 3D IFU model for minerals, shown in Fig.7.

3.4 Building 3D IFM.

Fig.8. show the detailed building process. Information on pore size distribution are obtained from scalable SEM images, whereas those on mineral content originate from the EDS images. We derive the fractal parameters for each mineral and build 3D IFU model for pores and minerals. As shown in Fig., the 3D IFU models for pores and for minerals overlap with each other. Thus, the pore walls will gain mineral properties. To simplify the fractal model, we assume that one pore wall gains only one mineral property, and one mineral gains only one wettability property (static contact angle). As a result, the minerals that gains the most proportion on one pore wall will give its mineral property on this pore wall. In this manner, each pore will receive one mineral characteristic. Finally, the 3D IFM can be successfully derived.

3.5 Relative permeability calculation

After the foundation of the 3D IFM, we extend Table 1 to contain mineral properties as Table 3. Within one iteration level,

the equivalent diameters are equal but share four different mineral properties. Therefore, this iteration level is extended into four

rows. Each row includes only one mineral, and the pore number in this row denotes the number of pores containing this mineral

on their walls. The sum pore number at this iteration level for all four minerals equals the pore number in the non-extended table.

The basic 3D IFM is similarly extended in this manner. As shown in Table, for example, N_2 number of pores is given for pores

with equivalent diameter λ_2; at the same time, λ_2 contains four kinds of mineral types with four different capillary pressures.

The table is initially rearranged in accordance with the descending order of pore diameters. Then, we rearrange the rows that share

the same diameter in accordance with the descending order of capillary pressure. The basic principle for relative permeability

calculation is the same between PCC table and extended PCC table. By following the PCC rules described before, it is convenient

to calculate residual oil saturation and relative permeability in the extended table for 3D IFM with mineral properties.

3.6 Model validation

The 3D IFM method for pore space representation was successfully verified in several works [43-44]. To verify the relative

permeability calculation, we use the published experimental data [59-60]. The validation between experimental data and 3D-IFM

calculation results are shown in Fig.9. The model results are generally close to the experimental data, which verify our 3D IFM

model. Also, our 3D IFM model is relatively open and applicable. As described, in the process for fractal representation for

micropores, SEM image is not the only information source for real pore size distribution. Other methods, like nuclear magnetic

resonance and CT image, are acceptable because different method has different best performance pore size range. Similarly, in

minerals representation process, when EDS test is not convenient to conduct, X-Ray powder diffraction method is also acceptable

when the mineral grain distribution in space is not something to be focused on. For different types of non-Darcy fluids, 3D IFM

model is also applicable, just slightly alter the base flowing behavior functions.

4 Application of 3D IFM: simple influencing factors of displacement

4.1 Pore size

In this section and the following section, we used the previous built 3D IFM for tight sandstone to investigate some important

influencing factors in multi displacement process. The first is pore size.

Pore size is a critical parameter in multiphase flow in tight sandstone. During micro displacement, flow behavior is

synthetically influenced by several forces, such as capillary force, floating force, and driving force. The average weight of these forces will change with increasing pore size. To simplify the driving process, we consider three forces as an example: capillary force, floating force, and driving force. Then, we normalize these forces using the following equation:

$$P_{cD} = P_c / P_{sum}, \ P_{FD} = P_F / P_{sum}, \ P_{fD} = P_f / P_{sum}, \tag{32}$$

where P_c and P_{cD} denote the capillary force and normalized capillary force, respectively. P_F and P_{FD} represent the driving force and normalized driving force, respectively. P_f and P_{fD} refer to the floating force and normalized floating force, respectively. The sum of these forces is $P_{sum} = P_c + P_F + P_f$. The normalized equivalent diameter is defined as follows:

$$\lambda_D = \lambda / L, \tag{33}$$

where λ and L are the equivalent diameter and length of the single pore, respectively. Shown in Fig.10, as the diameter of pore increases, the influence of capillary force decreases. In tight sandstone, the capillary force is a dominant force, whereas the influence of buoyant force increases with increasing pore diameter. According to calculations, in a single pore, the buoyant force is larger than the capillary force when normalized equivalent diameter surpass 10^{-6}, which is called the equilibrium point. In conventional sandstone, normalized equivalent diameter range is constantly at the right side of the equilibrium point, buoyant force has significant influence in multiphase flow. In tight sandstone, the influence of buoyant force is minimal compared with the other forces.

4.2 Oil–water viscosity ratio

Oil–water viscosity ratio is an important dimensionless parameter in tight oil development. A verity of parameters will influence oil–water viscosity ratio, like formation depth, temperature and asphalt content in oil. To focus on the ratio, we set the relative oil–water viscosity ratio ($\mu_r = \mu_o / \mu_w$) at 1, 5 and 10. Using the 3D IFM, we can calculate the relative permeability curve and displacement effect immediately. The result is shown in Fig.11. As the relative oil–water viscosity ratio increases, the isotonic point of relative permeability move to the left, relative permeability curve for oil also move to the left, indicating that the sandstone is more hydrophobic in general. More dense oil will resist in matrix after displacement, therefore, oil displacement efficiency Er_{o-w} will increase in primary drainage.

Mineral components will notably influence oil–water displacement, especially in tight sandstone. We simulate four types of mineral components in tight sandstone in the 3D IFM. Keeping the content of dolomite and orthoclase constant, we increase the percentage of quartz and decrease the percentage of albite, listed in Table 4. The results are shown in Fig.12. As the component of quartz increases, the isotonic point of relative permeability move to the right, relative permeability curve for water also move to the right. Based on several experiments, the hydrophilicity of quartz is relatively stronger than other minerals[61]. As the component of quartz increases, the simulated sandstone will become further hydrophilic, thereby increasing the irreducible water saturation. Finally, oil displacement efficiency Er_{o-w} will decrease.

5 Application of 3D-IFM: synthetic influencing factors of displacement

Multiphase flow in formation is a complicated process. Factors, such as pore compression, mineral component, wettability ageing and compound forces, will influence multiphase displacement process synthetically. Here, we make a simple model to simulate synthetic influencing factors on multiphase displacement at different formation depth. With the increase in reservoir depth, the temperature of formation will increase, thereby decreasing oil viscosity, threshold pressure and formation pressure, subsequently influencing the relative permeability curve and displacement effect synthetically. To simulate multi-flow in different depths and investigate synthetic influences on multi-flow, we define four depth increases from 1500 m to 6000 m. The viscosity-temperature curve comes from experimental data by Zhang et al.[59], geothermal gradient is 2.1°C/100 m according to the collected formation data from Xinjiang Basin. Using the 3D IFM, we can calculate the relative permeability curve and displacement effect immediately. The results are shown in Fig.13. With the increase in formation depth, the isotonic point of relative permeability move to the right, relative permeability curve for oil also move to the right. The reason is the viscosity of oil at formation will decrease as formation depth increase, oil are easier to flow, thereby maybe diminishing the fingering effect. Therefore, in deep formation, oil displacement efficiency Er_{o-w} will decrease.

6 Conclusions

A rapid relative permeability evaluation method for tight sandstone based on 3D IFM is introduced. Initially, a revised 3D IFM is built on the basis of high-resolution SEM and EDS images of tight sandstones with pores exhibiting mineral properties.

Then, we develop a PCC method to calculate the relative permeability and residual oil saturation of the 3D IFM. The accuracy of

this model is verified by both experimental and simulated data, indicating that this method satisfactorily evaluates multiphase displacement in tight sandstone. Finally, as an application of 3D IFM method, the influences of several factors on multiphase displacement efficiency are discussed, including oil–water viscosity ratio, mineral components. Also, the synthetic influence by several factors. On displacement behavior is discussed.

The findings show that the modified 3D IFM is valid and useful. By using the self-similar properties, the expression process of pore size distribution and mineral properties is simplified, thereby providing a solid foundation for relative permeability calculation. From the simulation results, as oil-water viscosity ratio increase, the oil-water displacement efficiency will increase. And as the content of hydrophilic mineral decrease, the oil-water displacement efficiency will increase. In addition, the revised 3D IFM based on PCC method can rapidly evaluate the multiphase displacement process. This method provides another efficient way to research multiphase flow and shows a potential application for future use.

Nomenclature

A	=	cross-sectional area, m^2
C	=	shape factor
C_a	=	capillary number
C_i	=	shape factor for capillary at iteration level i
$\tilde{C}_n$	=	curvature of a meniscus,
Er_{o-w}	=	displacement efficiency for oil displace water
i	=	iteration level in IFU model
$k_{nw\_sub}(i)$	=	non-wetting phase permeability at iteration level i
$k_{w\ sub}(i)$	=	wetting phase permeability at iteration level i
L	=	the edge length of model, m
L_p	=	distance from cross section to pressure inlet,m
N_i	=	number of pores generated at iteration level i
N_{i_Mj}	=	number of pores with j th mineral and Pore diameter λi
P_1	=	fraction of connecting pores
$P_{1.i}$	=	fraction of connecting pores (except dead ends) existing at i th iteration level
$P_{1,i\ Mj}$	=	fraction of connecting poresexisting at i th iteration level with j th mineral
P_2	=	traverse probability
$P_{2,i \to i}$	=	traverse probability from pore neck at iteration level i to iteration level j.
P_c	=	capillary pressure, Pa
P_{cD}	=	normalized capillary force
P_{CSDP}	=	connecting and successful displacement probability
$P_{CSDP,i}$	=	connecting and successful displacement probability for iteration level i
P_F	=	driving force, Pa
P_{FD}	=	normalized driving force
P_f	=	floating force, Pa

P_{fD}	=	normalized floating force
P_G	=	projection of gravity on flow direction, Pa
$P_{initial}$	=	the threshold pressure gradient, Pa
$S_{wres}(\alpha, \theta_R, i)$	=	residual wetting phase at iteration level i
$S_{nw\ sub}(i)$	=	non-wetting phase residual saturation at iteration level i

α	=	half angle of the corner,°
θ_{ea}	=	static contact angle,°
θ_R	=	dynamic contact angle,°
λ	=	equivalent tube diameter for capillary tube, m
λ_i	=	equivalent tube diameter for IFU model at iteration level i, m
λ_D	=	normalized equivalent diameter
μ_{nw}	=	viscosity of non-wetting phase, Pa.s
μ_w	=	viscosity of wetting phases, Pa.s
σ	=	interfacial tension between two fluid phases
φ_i	=	percentage of mineral component i

Acknowledgements

Additional Information

Competing interests statement: the authors declare that they have no competing financial interests.

References

[1] Masters JA. Deep Basin Gas Trap, Western Canada. AAPG Bull 1979;63(2):152. https://doi.org/ 10.1306/c1ea55cb-16c9-11d7-8645000102c1865d.

[2] Spencer CW. Review of characteristics of low-permeability gas reservoirs in western United States. AAPG Bull 1989;73(5):613-629. https://doi.org/10.1306/44b4a23a-170a-11d7-8645000102c1865d.

[3] Nelson PH. Pore-throat sizes in sandstones, tight sandstones, and shales. AAPG Bull. 2009;93(3):329-340. https://doi.org/10.1306/10240808059

[4] Higgs KE, Zwingmann H and Reyes AG, Diagenesis, porosity evolution, and petroleum emplacement in tight gas reservoirs, Taranaki basin, New Zealand. J Sediment Res 2007;77:1003–1025. https://doi.org//10.2110/jsr.2007.095

[5] Li Z., Duan Y., Fang Q., Wei, M. A study of relative permeability for transient two-phase flow in a low permeability fractal porous medium. Adv. Geo-Energy Res., 2018; 2(4): 369-379 https://doi.org//10.26804/ager.2018.04.02.

[6] Cai J., Lin D, Singh H, et al. Shale gas transport model in 3D fractal porous media with variable pore sizes. Marine and Petroleum Geology, 2018, 98: 437-447. https://doi.org/10.1016/j.marpetgeo.2018.08.040.

[7] Wang F, Yang K, Cai J. Fractal characterization of tight oil reservoir pore structure using nuclear magnetic resonance and mercury intrusion porosimetry. Fractals, 2018, 26(02): 1840017. https://doi.org/10.1142/S0218348X18400170.

[8] Tian F, Wang W , Liu N , et al. Rock-Type Definition and Pore Characterization of Tight Carbonate Rocks Based on Thin Sections and MICP and NMR Experiments. Appl. Magnetic Res., 2018, 49(1):1-22. https://doi.org/10.1007/s00723-018-0993-2.

[9] Tian F, Di Q , Jin Q , et al. Multiscale geological-geophysical characterization of the epigenic origin and deeply buried paleokarst system in Tahe Oilfield, Tarim Basin. Marine and Petroleum Geology, 2019. 102: 16-22. https://doi.org/10.1016/j.marpetgeo.2018.12.029.

[10] Chen, P., Miska, S. Z., Ren, R., Yu, M., Ozbayoglu, E., & Takach, N. (2018). Poroelastic Modeling of Cutting Rock in Pressurized Condition. J Petro Sci Eng, 169, 623-635. https://doi.org/10.1016/j.petrol.2018.06.009

[11] Fatt I. The Network Model of Porous Media. I. Capillary Pressure Characteristics. Pet Trans AIME 1956;207:144-159. SPE-574-G. http://dx.doi.org/10.2118/SPE-574-G.

[12] Bryant S, and Blunt M. Prediction of Relative Permeability in Simple Porous Media. Phys Rev A 1992;46(4): 2004-2011. https://doi.org/10.1103/physreva.46.2004.

[13] Bryant S, Cade C, and Mellor D. Permeability Prediction from Geologic Models. AAPG Bull 1993;77(8): 1338-1350. https://doi.org/10.1306/bdff8e84-1718-11d7-8645000102c1865d.

[14] Blunt M. Effects of heterogeneity and wetting on relative permeability using pore level modeling. SPE J 1997;2 (01): 70–87. https://doi.org/10.2118/36762-PA

[15] Mani V, and Mohanty K. Pore-level network modeling of three-phase capillary pressure and relative permeability curves. SPE J 1998;3 (03):238–248 . https://doi.org/10.2118/50942-PA

[16] Dixit A, McDougall S, and Sorbie K. A pore-level investigation of relative permeability hysteresis in water-wet systems. SPE J 1998;3 (02):115–123 . https://doi.org/10.2118/37233-PA

[17] Fischer U, and Celia MA. Prediction of Relative and Absolute Permeabilities for Gas and Water from Soil Water Retention Curves Using a Pore-Scale Network Model. Water Resour Res 1999;35(4): 1089-1100. https://doi.org/10.1029/1998wr900048.

[18] Valvatne PH, and Blunt MJ. Predictive pore-scale modeling of two-phase flow in mixed wet media. Water Resour Res 2004;40(7) https://doi.org/10.1029/2003wr002627

[19] Yuan B, Moghanloo GR, Zheng D. et al. A. Novel Integrated Production Analysis Workflow for Evaluation, Optimization and Predication in Shale Plays. Int. J. Coal Geol. 2017;180:18-28. https://doi.org/10.1016/j.coal.2017.04.014.

[20] Lu T, Li Z, Lai F, et al. The effect of flow resistance on water saturation profile for transient two-phase flow in fractal porous media. Adv. Geo-Energy Res. 2018;2(1):63-71. https://doi.org/10.26804/ager.2018.01.06.

[21] Bakke S, and Øren PE. 3-D pore-scale modelling of sandstones and flow simulations in the pore networks. SPE J 1997; 2(02): 136–149. https://doi.org/10.2118/35479-PA

[22] Nguyen VH, Sheppard AP, Knacksted, MA, et al. The effect of displacement rate on imbibition relative permeability and residual saturation. J Petro Sci Eng 2006;52(1):54-70. https://doi.org/10.1016/j.petrol.2006.03.020

[23] Ren X, Li A, Fu S. et al. Experimental study on the oil-water relative permeability relationship for tight sandstone considering the nonlinear seepage characteristics. J. Petro. Sci. Eng. 2018;161:409-416. https://doi.org/10.1016/j.petrol.2017.12.003

[24] Katz AJ and Thompson AH, Fractal sandstone pores: implications for conductivity and pore formation. Phys Rev Lett 1985;54(12):1325. https://doi.org/10.1103/PhysRevLett.54.1325

[25] Erzan A, and Güngör N. Fractal geometry and size distribution of clay particles. J colloid int Sci 1995;176(2): 301-307. https://doi.org/10.1006/jcis.1995.9963

[26] Yu BM. and Li JH, Some Fractal Characters of Porous Media. Fractals 2001;9(3): 365-372. https://doi.org/10.1142/s0218348x01000804.

[27] Yu BM. Fractal Character for Tortuous Streamtubes in Porous Media. Chin Phys Lett 2005;22 (1): 158-160. https://doi.org/10.1088/0256-307x/22/1/045.

[28] Toledo PG, Novy RA, Davis HT, et al. Capillary pressure, water relative permeability, electrical conductivity and capillary dispersion coefficient of fractal porous media at low wetting phase saturations. SPE Adv Tech Series 1994;2(01): 136-141. https://doi.org/10.2118/23675-pa

[29] Cai J, Yu B, Zou M. et al. Fractal Characterization of Spontaneous Co-current Imbition in Porous Media. Energy & Fuels 2010;24(3): 1860-1867. https://doi.org/10.1021/ef901413p.

[30] Cai J. A Fractal Approach to Low Velocity Non-Darcy Flow in a Low Permeability Porous Medium. Chinese Phys B 2014;23(4): 044701. https://doi.org/10.1088/1674-1056/23/4/044701.

[31] Cai J, Perfect E, Cheng C. et al. Generalized modeling of spontaneous imbibition based on Hagen-Poiseuille flow in tortuous capillaries with variably shaped apertures. Langmuir 2014; 30(18):5142-5151. https://doi.org/10.1021/la5007204

[32] Xiao B, Fan J, and Ding F. Prediction of relative permeability of unsaturated porous media based on fractal theory and Monte Carlo simulation. Energy Fuels 2012;26(11): 6971-6978. https://doi.org/10.1021/ef3013322

[33] Xu P, Qiu S, Yu B, et al. Prediction of relative permeability in unsaturated porous media with a fractal approach Int. J Heat Tran 2013;64: 829-837. https://doi.org/10.1016/j.ijheatmasstransfer.2013.05.003

[34] Lei G, Dong P, Wu Z. et al. A fractal model for the stress-dependent permeability and relative permeability in tight sandstones. J Can Petro Tech 2015;54(01): 36-48. https://doi.org/10.2118/173897-pa

[35] Balankin AS, and Elizarraraz BE. Hydrodynamics of fractal continuum flow. Phys Rev E 2012; 85(2-2):025302. https://doi.org/10.1103/PhysRevE.85.025302.

[36] Balankin AS, and Elizarraraz BE. Map of fluid flow in fractal porous medium into fractal continuum flow. Phys Rev E 2012;85(5): 056314. https://doi.org/10.1103/PhysRevE.85.056314.

[37] Pia G, and Sanna U. Geometrical Fractal Model for the Porosity and Thermal Conductivity of Insulating. Concrete Constr Build Mater 2013;44(44): 551–556. https://doi.org/10.1016/j.conbuildmat.2013.03.049.

[38] Pia G, and Sanna U. Intermingled Fractal Units Model and Electrical Equivalence Fractal Approach for Prediction of Thermal Conductivity of Porous Materials Appl Therm Eng 2013;61(2):186-192. https://doi.org/10.1016/j.applthermaleng.2013.07.031.

[39] Pia G, and Sanna U. An Intermingled Fractal Units Model and Method to Predict Permeability in Porous Rock. Int J of Eng Sci 2014:75(2): 31–39. https://doi.org/10.1016/j.ijengsci.2013.11.002.

[40] Pia G. Fluid Flow in Complex Porous Media: Experimental Data and IFU Model Predictions for Water Vapour Permeability. J Nat Gas Sci Eng 2016;35:283-290. https://doi.org/10.1016/j.jngse.2016.08.053.

[41] Cihan A, Tyner JS, and Perfect E. Predicting relative permeability from water retention: a direct approach based on fractal geometry. Water Resour Res 2009;45(4):W04404. https://doi.org/10.1029/2008WR007038.

[42] Cihan A, Sukop MC, Tyner JS, et al. Analytical Predictions and Lattice Boltzmann Simulations of Intrinsic Permeability for Mass Fractal Porous Media. Vadose Zone J 2009;8(1):187. https://doi.org/10.2136/vzj2008.0003.

[43] Li C, Lin M, and Ji L, et al. Rapid Evaluation of the Permeability of Organic-Rich Shale Using the 3D Intermingled-Fractal Model. SPE J 2018;191358-PA https://doi.org/10.2118/191358-PA.

[44] Cihan A, Perfect E, and Tyner JS. Water Retention Models for Scale-Variant and Scale-Invariant Drainage of Mass Prefractal Porous Media. Vadose Zone J 2007;6(4):786. https://doi.org/10.2136/vzj2007.0062er

[45] Marshall TJ. A Relation between Permeability and Size Distribution of Pores. J Soil Sci 1958;9:1–8. https://doi.org/10.1111/j.1365-2389.1958.tb01892.x

[46] Tian W, Li A, Ren X, et al. The threshold pressure gradient effect in the tight sandstone gas reservoirs with high water saturation. Fuel 2018;226:221-229. https://doi.org/10.1016/0927-7757(96)03702-8

[47] Ma S, Mason G, Morrow NR. Effect of contact angle on drainage and imbibition in regular polygonal tubes. Coll Surf A 1996;117(3):273-291. https://doi.org/10.1016/0927-7757(96)03702-8

[48] Hilpert M, Effects of dynamic contact angle on liquid infiltration into horizontal capillary tubes: (semi)-analytical solutions. J Colloid Interf Sci 2009;337:131–137. https://doi.org/10.1016/j.jcis.2009.04.013

[49] Hilpert M, Effects of dynamic contact angle on liquid infiltration into inclined capillary tubes: (Semi)-analytical solutions. J. Colloid Interf Sci 2009;337:138–144. https://doi.org/10.1016/j.jcis.2009.04.058

[50] Hilpert M, Effects of dynamic contact angle on liquid withdrawal from capillary tubes: (semi)-analytical solutions. J Colloid Interf Sci 2010;347:315–323. https://doi.org/10.1016/j.jcis.2010.03.055

[51] Hilpert M, Explicit analytical solutions for liquid infiltration into capillary tubes: Dynamic and constant contact angle. J Colloid Interf Sci 2010;344:198–208. https://doi.org/10.1016/j.jcis.2009.12.024

[52] Hilpert M, Liquid withdrawal from capillary tubes: explicit and implicit analytical solution for constant and dynamic contact angle. J Colloid Interf Sci 2010;351:267–276. https://doi.org/10.1016/j.jcis.2010.07.016

[53] Piri M and Blunt MJ. Three-dimensional mixed-wet random pore-scale network modeling of two- and three-phase flow in porous media. I. Model description, Phys Rev E 2005;71:026301. https://doi.org/10.1103/physreve.71.026302

[54] Meakin P, Tartakovsky AM. Modeling and simulation of pore-scale multiphase fluid flow and reactive transport in fractured and porous media. Rev Geo 2009;47(3) https://doi.org/10.1029/2008rg000263

[55] Raeini AQ, Bijeljic B, and Blunt MJ. Numerical modelling of sub-pore scale events in two-phase flow through porous media. Trans porous med 2014;101(2):191-213. https://doi.org/10.1016/0927-7757(96)03702-8

[56] Joekar-Niasar V, Hassanizadeh SM. Analysis of Fundamentals of Two-Phase Flow in Porous Media Using Dynamic Pore-Network Models: A Review. Critic. Rev Env Sci Tech 2012;42(18):1895-1976. https://doi.org//10.1080/10643389.2011.574101

[57] Veltzke T, and Thöming J. An Analytically Predictive Model for Moderately Rarefied Gas Flow J Fluid Mech

2012;698 (5): 406-422. https://doi.org/10.2118/39219-ms.

[58] Li C, Lin M, Ji L, et al. Investigation of Intermingled Fractal Model for Organic-Rich Shale. Energy & Fuels 2017;31(9): 8896-8909. https://doi.org/10.1021/acs.energyfuels.7b00834.

[59] Zhang LH, Tong J, Xiong Y, et al. Effect of temperature on the oil–water relative permeability for sandstone reservoirs. Int J Heat Mass Trans 2017; 105:535-548. https://doi.org/10.1016/j.ijheatmasstransfer.2016.10.029

[60] Oak MJ. Three-phase relative permeability of water-wet Berea. SPE Enhanced Oil Recovery Symposium. 1990;109-120. https://doi.org/10.2523/20183-ms

[61] Wu C, Xue H, Lu S. et al. Measurement and Analysis of Oil-water Contact Angle on Several Common Minerals. Geoscience, 2018;32(4):842-849. https://doi.org/10.19657/j. geoscience.1000－8527.2018.04.20

Tables

Table 1

Connecting probability calculation process.

Iteration level (i)	Pore diameter	Number of pores	connected fraction	Connecting and successful displacement probability
1	λ_1	N_1	$P_{1,1}$	$\dfrac{\lambda_1^2 <N_1 P_{1,1}>}{A} \dfrac{\lambda_1^2 <N_1 P_{1,1}>}{A} P_{2,1\to 1}$
2	λ_2	N_2	$P_{1,2}$	$\dfrac{\lambda_2^2 <N_2 P_{1,2}>}{A} \dfrac{\lambda_2^2 <N_2 P_{1,2}>}{A} P_{2,2\to 2} +$ $\dfrac{\lambda_1^2 <N_1 P_{1,1}>}{A} \dfrac{\lambda_2^2 <N_2 P_{1,2}>}{A} P_{2,1\to 2} + \dfrac{\lambda_1^2 <N_1 P_{1,1}>}{A} \dfrac{\lambda_2^2 <N_2 P_{1,2}>}{A} P_{2,2\to 1}$
…	…	…	…	…
n	λ_n	N_n	$P_{1,n}$	$\dfrac{\lambda_n^2 <N_n P_{1,n}>}{A} \dfrac{\lambda_n^2 <N_n P_{1,n}>}{A} P_{2,n\to n} +$ $\sum_{i-1}^{n} \dfrac{\lambda_i^2 <N_i P_{1,i}>}{A} \dfrac{\lambda_n^2 <N_n P_{1,n}>}{A} (P_{2,i\to n} + P_{2,n\to i})$

Table 2

IFU model input data for pores in sandstone.

	Unit A	Unit B	Unit C
Df	1.89	1.63	1.26
n unit	1	35	6000
n pore(i=1)	1	3	5
λ_{max} (nm)	18420	6500	780
Iteration	5	4	3
λ_{min} (nm)	227.4	75.8	86.66
Solid forever	0	0	0
total surface(μm^2)		512656	
$\varepsilon_{SEM} / \varepsilon_{IFU}$		0.082/0.082	

Table 3

Extended connecting probability calculation table

Pore diameter	Mineral type	Number of pores	connected fraction	Capillary pressure
λ_1	quartz	N_{1_M1}	$P_{1,1\_M1}$	$P_{c\_1,1\_M1}$
λ_2	quartz	N_{2_M1}	$P_{1,2\_M1}$	$P_{c\_1,2\_M1}$
λ_2	albite	N_{2_M2}	$P_{1,2\_M2}$	$P_{c\_1,2\_M2}$
λ_2	dolomite	N_{2_M3}	$P_{1,2\_M3}$	$P_{c\_1,2\_M3}$
λ_2	orthoclase	N_{2_M4}	$P_{1,2\_M4}$	$P_{c\_1,2\_M4}$
λ_3	quartz	N_{3_M1}	$P_{1,3\_M1}$	$P_{c\_1,3\_M1}$
…	…	…	…	…

Table 4

Mineral components for the three cases

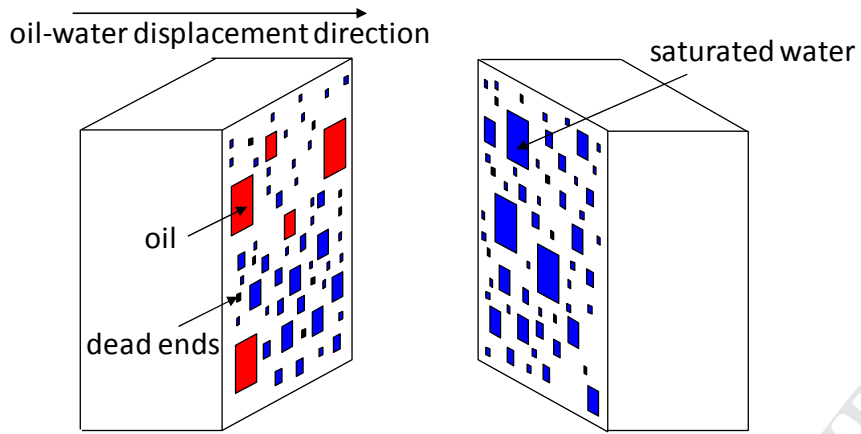|	φ_{quartz}	φ_{albite}	$\varphi_{dolomite}$	$\varphi_{orthoclase}$
Case1	40%	57%	2%	1%
Case2	60%	37%	2%	1%
Case3	80%	17%	2%	1%

Fig. 1. Connecting probability calculation model for multiphase displacement
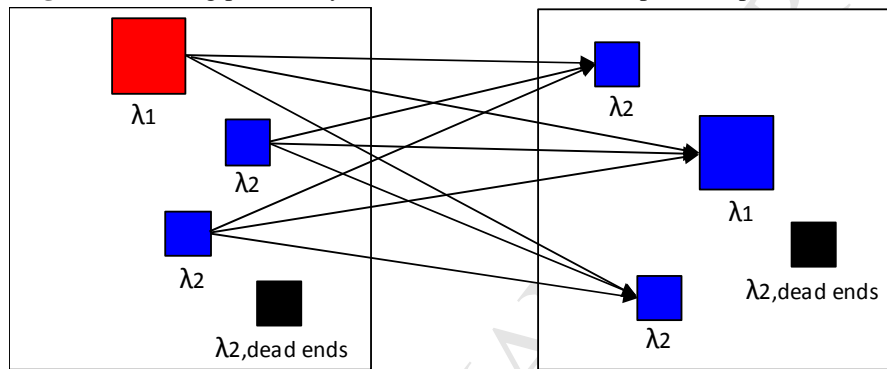
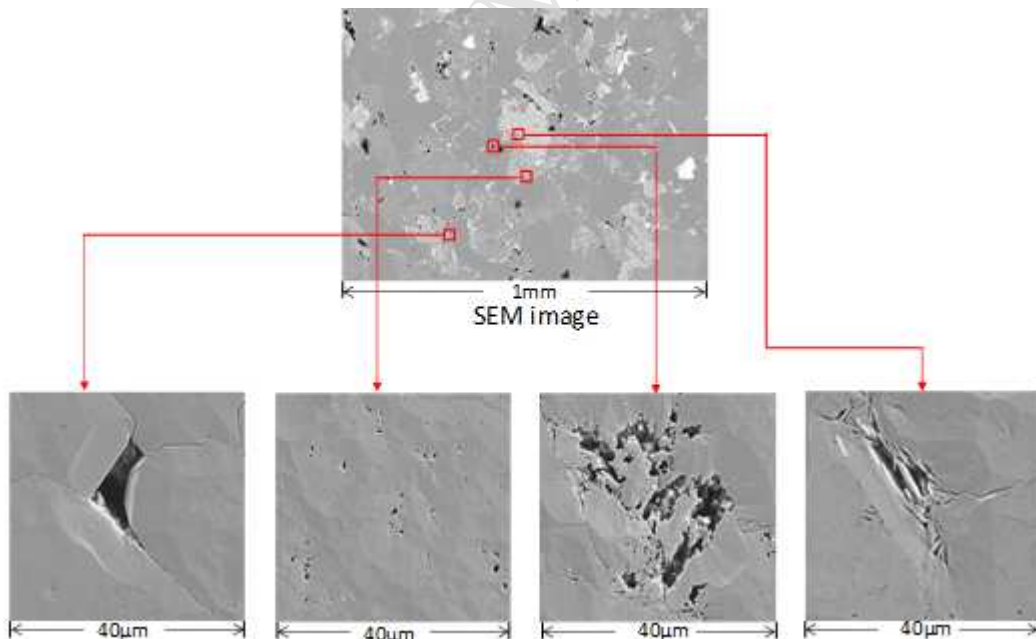**Fig. 2.** Schematic of pore connective calculation method
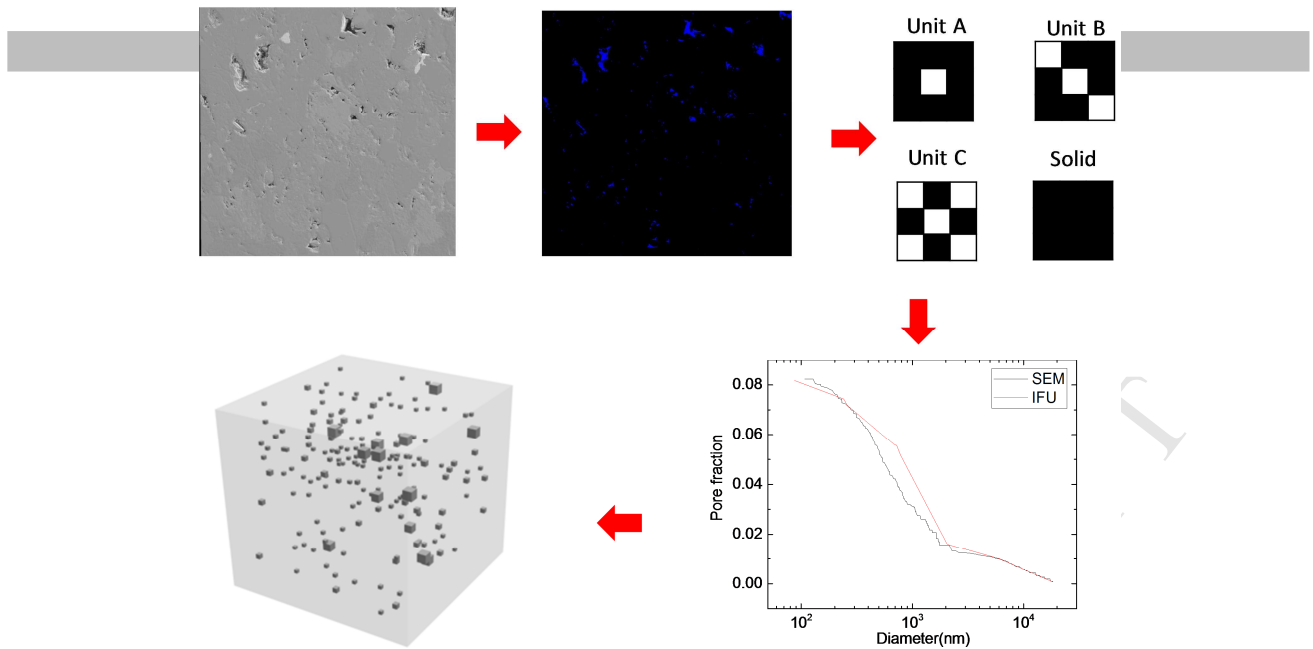

Fig. 3. SEM image of Xinjing tight sandstone

Fig. 4. Fractal representation for micropores
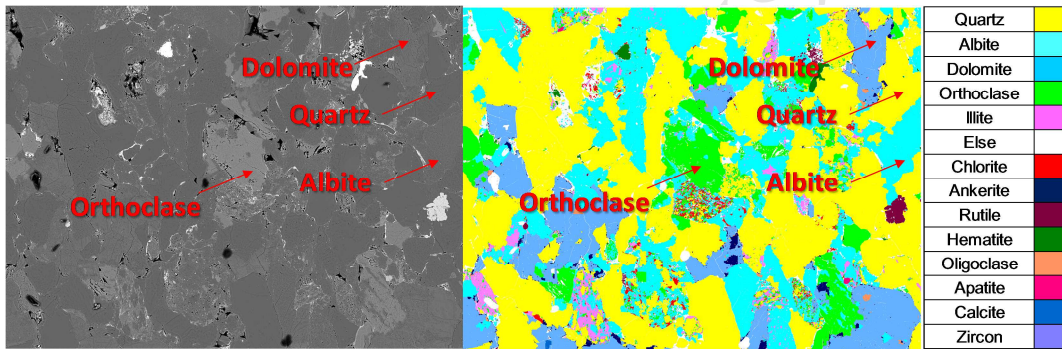
Fig. 5. EDS results for tight sandstone
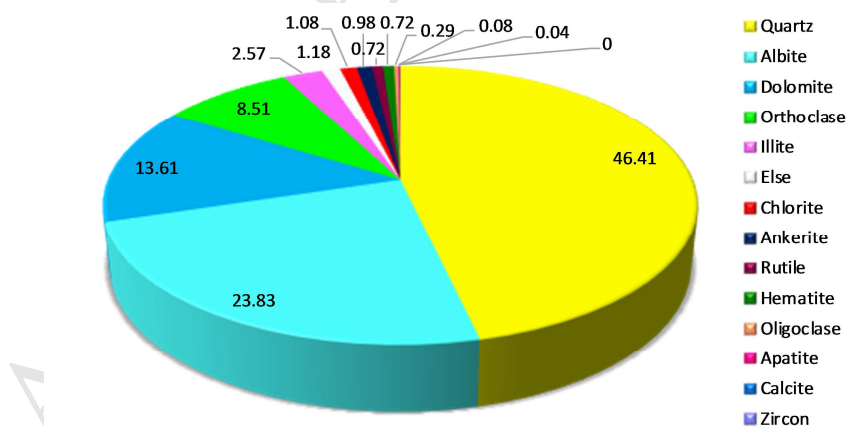
Fig. 6. Statistics for minerals from EDS results
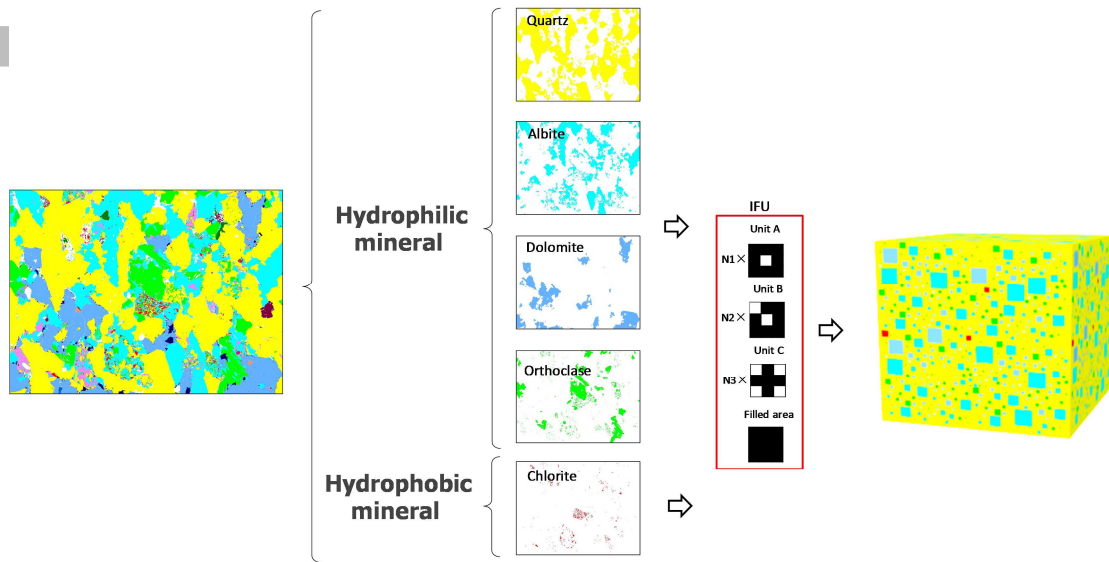
Fig. 7. Fractal representation for minerals
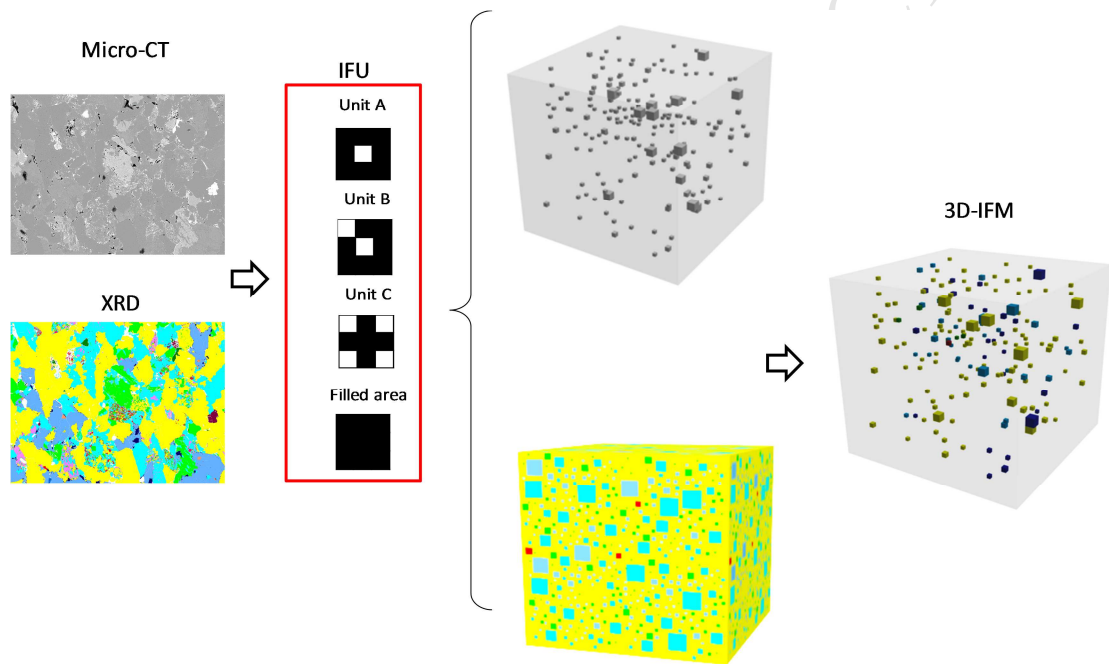
Fig.8. IFM procedure for tight sandstone

(a)

(b)
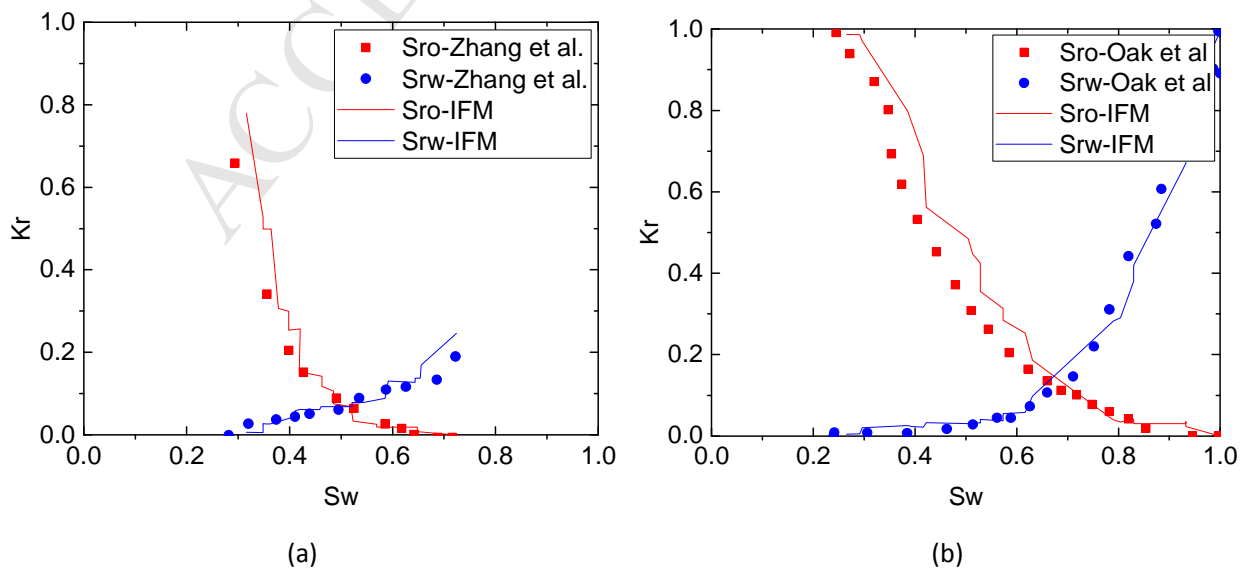
Fig. 9. Model validation for 3D IFM
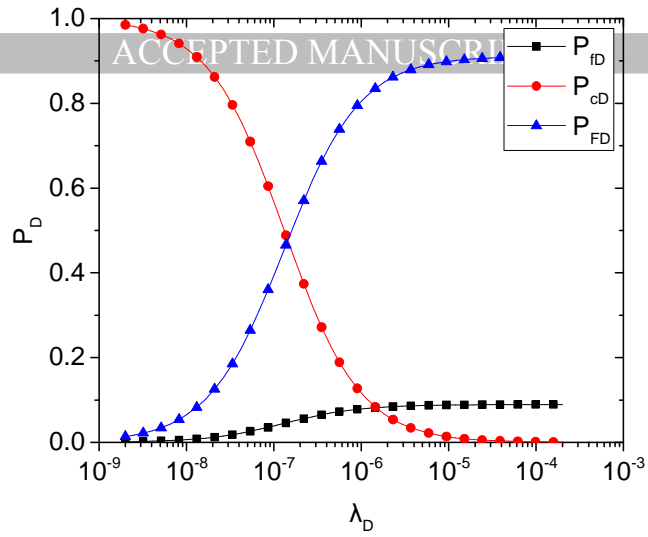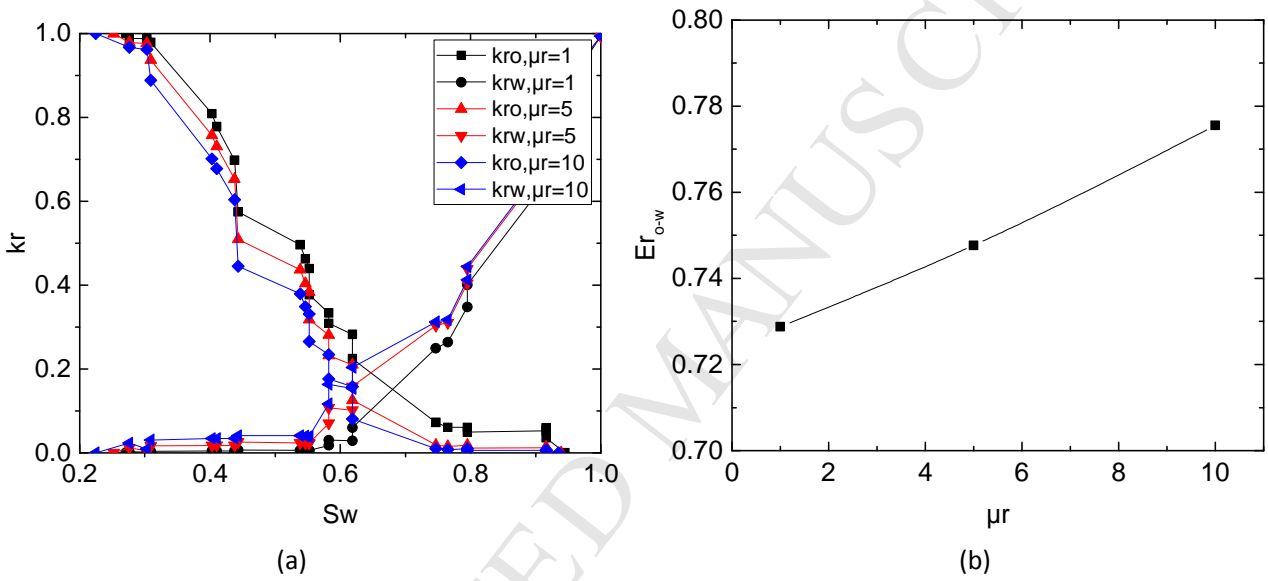
Fig.10. The influence of pore size on several forces

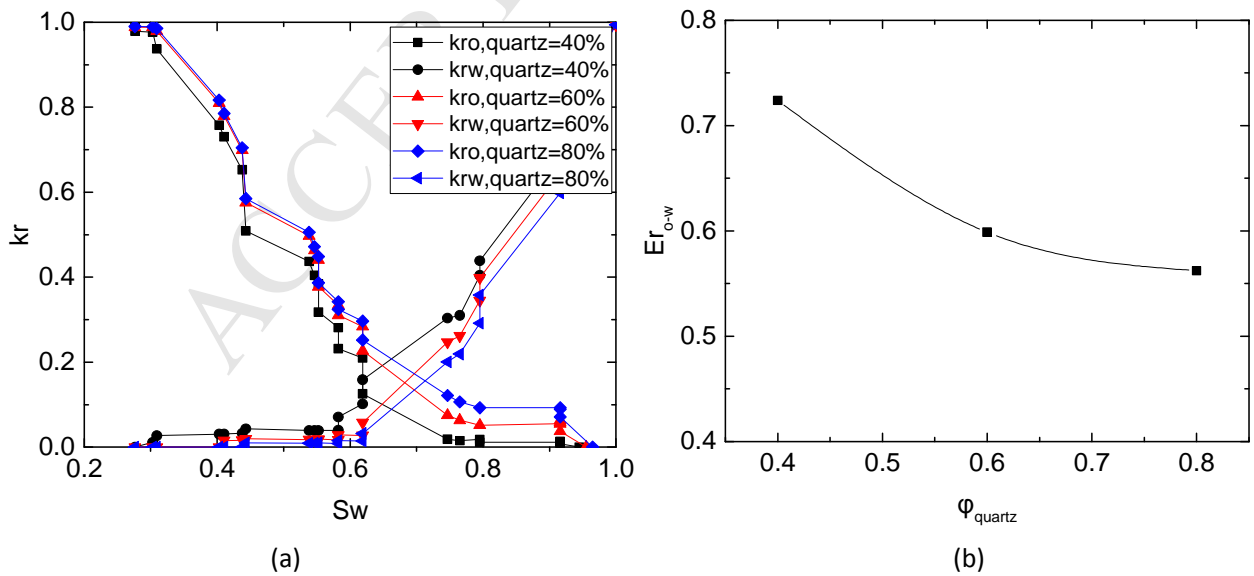**Fig. 11.** The influence of Oil–water viscosity ratio on displacement behavior

Fig. 12. The influence of mineral components on displacement behavior
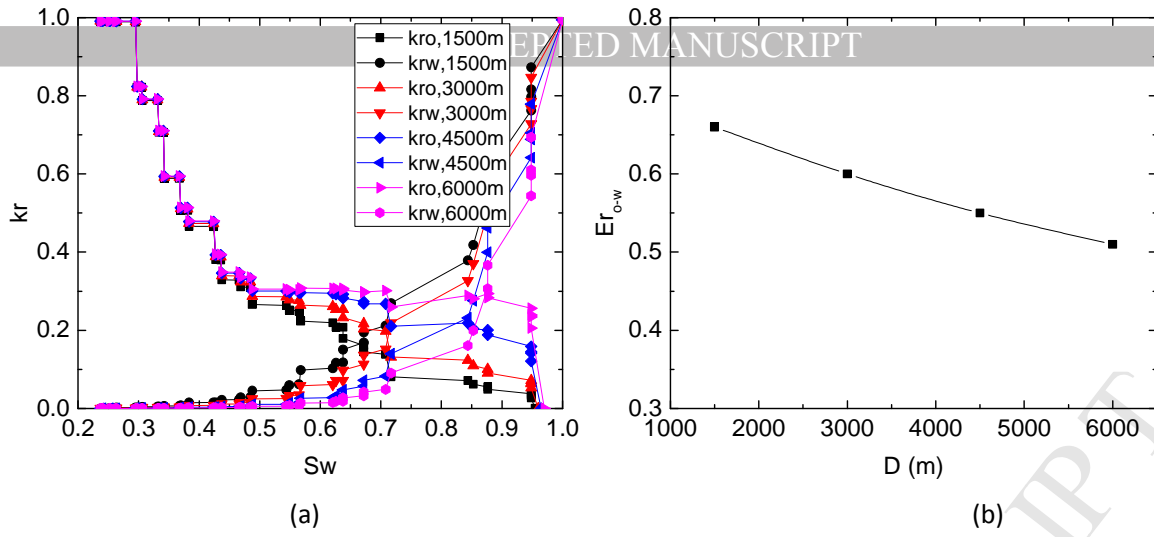
(a)　　　　　　　　　　　　　　　　　　　(b)

Fig.13. Synthetic influence on displacement behavior

Highlights

•An advanced 3D intermingled fractal method is used to Multiphase flow in tight sandstone .

•Fractal characteristics of pore size distribution and mineral grain distribution are derived from real images from tight sandstone.

•This method is useful and reliable for calculating relative permeability, with main influencing factors included and fast evaluating process.